



## Full Text View

[Volume 32, Issue 10 \(October 2002\)](#)
**Journal of Physical Oceanography**

 Article: pp. 2789–2805 | [Abstract](#) | [PDF \(1.06M\)](#)

## Baroclinic Eddy Interaction with Isolated Topography

**William K. Dewar**
*Department of Oceanography, The Florida State University, Tallahassee, Florida*

(Manuscript received November 15, 2000, in final form March 1, 2002)

DOI: 10.1175/1520-0485(2002)032&lt;2789:BEIWIT&gt;2.0.CO;2

**ABSTRACT**

Point vortex and finite-difference methods are used to study baroclinic eddies advected into weak and strong encounters with topography. It is argued that weak interactions often scatter radially symmetric eddies into generalized hetons. The dipole moments so generated within the eddy result in eddy propagations at various angles to the current. Strong interactions can result in the complete separation of the upper- and lower-layer circulations. Subsequent evolution in this case depends on many factors, although strong topographic obstacles (i.e., seamounts) permit a reorganization of the centers into a coherent structure. Weaker topography, confined to the deep ocean, can disrupt the lower center, although the upper center typically survives. Disassociation of the centers with both retaining their integrity is also possible. Heton generation can occur for eddies with weak lower-layer expressions, demonstrating a potentially strong control of shallow eddy propagation by deep sea bathymetry. Analytical and numerical estimates of the induced propagation speeds are sizable, arguing topographic scattering is a potentially powerful mechanism influencing eddy propagation.

**1. Introduction**

Observations suggest that the ocean is heavily populated with subsurface vortices ([Ebbesmeyer et al. 1986](#)). If true, the implications of these vortices for property transport and mixing are profound. A particular and well-observed example of such eddies are those of Mediterranean origin (nicknamed “meddies”), and it is thought that they routinely undergo encounters with seamounts ([Richardson et al. 2000](#)). A limited amount of “before” encounter and “after” encounter data is available on such meddies, suggesting topographic interactions are disruptive and possibly fatal. This is important to gauging tracer transport by meddies. In addition, the ubiquity of bottom topography combined with the apparent number of subsurface vortices throughout the world ocean suggests vortex–topography interaction should be a commonplace event. The objectives of this paper are to numerically and theoretically study the problem of eddy–topography and eddy–seamount interaction to aid in the understanding and interpretation of observations.

*a. Background*

[Ebbesmeyer et al. \(1986\)](#) in their analysis of North Atlantic hydrographic data along 70°W suggested subsurface vortices, with a North Atlantic population estimated at 10 000, are a dominant form of ocean variability. Further, they showed that

## Table of Contents:

- [Introduction](#)
- [Isolated vortices in](#)
- [Baroclinic vortices near](#)
- [Vortex interactions with](#)
- [Discussion](#)
- [REFERENCES](#)
- [APPENDIX](#)
- [FIGURES](#)

## Options:

- [Create Reference](#)
- [Email this Article](#)
- [Add to MyArchive](#)
- [Search AMS Glossary](#)

## Search CrossRef for:

- [Articles Citing This Article](#)


## Search Google Scholar for:

- [William K. Dewar](#)

these vortices are often composed of water types along which they are embedded. This both makes these eddies, sometimes called SCVs (for submesoscale coherent vortices: see [McWilliams 1985](#)), easily identifiable and of potentially great significance to the mixing and transport of ocean properties. The reason SCVs house such distinct water types can be partially ascribed to their tendency to form near fronts between neighboring water masses. This is characteristic of perhaps the most widely recognized SCV in the World Ocean, the so-called meddy (i.e., an SCV of Mediterranean origin). [Richardson et al. \(2000\)](#) give a recent review of meddy observations.

Meddies, found mostly in the eastern midlatitude North Atlantic, are routinely composed of warm, salty waters relative to the background North Atlantic water type at their 1000-m equilibrium depth. A famous meddy observation, indeed perhaps the first, was made by [McDowell and Rossby \(1978\)](#) in the western North Atlantic, suggesting meddy survival over a 6000-km transit, probably requiring several years to complete. [Note however, the interpretation of this observation is under current debate ([Prater and Rossby 1999](#))].

Early meddy life histories are dominated by northward movement along the Iberian Peninsula and ejection into the Iberian basin either at Cape St. Vincent or the Tejo Plateau. They thereafter follow a curving trajectory, of about  $0.02 \text{ m s}^{-1}$  propagation amplitude, that brings them into the vicinity of the Horseshoe Seamounts. [Richardson et al. \(2000\)](#) suggest 70% of these meddies interact with the Horseshoe Seamounts and experience major structural distortion as a result. The remainder skirt north of the topography and enter into the Canary Basin. Of those interacting with the seamounts, it is not unusual for some part of them to survive, also to enter into the Canary Basin.

Typical meddy life histories in the Canary Basin fall mostly into one of three categories ([Richardson and Tychensky 1998](#)). The least active meddy history belongs to those that move south in the eastern North Atlantic. These have been observed to slowly decay, due to a variety of processes, and eventually dissipate ([Armi et al. 1989](#)). Second, many meddies interact with the Azores Current. Their subsequent evolution can be complicated, but survival of the encounter is routine. These meddies can follow an open-ocean route toward the Mid-Atlantic Ridge, and may be the family from which the McDowell and Rossby Meddy came. The third class are those that move dominantly southwestward and as a result encounter the Great Meteor seamount chain. This chain is composed of several major seamounts extending through the part of the water column occupied by the meddies, as well as many smaller topographic irregularities. [Figure 1](#)  contains a view of the Great Meteor seamounts, looking westward from the coast of Africa. The depth and size of a typical meddy are also shown by the oval. The latter figure enforces that interaction with seamounts of southwestward-moving meddies is almost an inevitability. Indeed, [Richardson et al. \(2000\)](#) estimate that between the Horseshoe and Great Meteor seamount chains, 90% of the meddy population encounter seamounts. Typical seamount diameters and separations are on the order of 50–100 km, which is also comparable to the diameter of meddies. Typical meddy speeds are also about  $0.02 \text{ m s}^{-1}$  ([Richardson et al. 2000](#)).

Many, but not all, float-based observations of meddies suggest their interactions with seamounts are very disruptive and perhaps fatal ([Richardson and Tychensky 1998](#); [Shapiro et al. 1995](#)). If this is true, such interactions become significant to the salt budget of the North Atlantic Mediterranean tongue. As Mediterranean salt is a major input to water masses in general (e.g., the North Atlantic Deep Water), understanding the source, sink, and transport mechanisms for the Mediterranean outflow finds motivation.

Other types of SCVs have been less well defined observationally. Nonetheless, the ocean bottom is rough and SCVs are apparently ubiquitous, so it is plausible that subsurface vortex interactions with seamounts and other topography are routine. Recent examples of such interactions in the South Atlantic are given in [Weatherly et al. \(2002\)](#).

The dynamical understanding of such interactions, however, is relatively poorly developed, a point noted by [Richardson et al. \(2000\)](#). Vortex topography–interaction has benefited from some numerical studies, often involving rings and continental slopes ([Louis and Smith 1982](#); [Smith 1986](#); Yasuda et al. 1996), but much less from laboratory, analytical, or process-oriented dynamical studies. Exceptions are [Carnevale et al. \(1991\)](#) and [Stern \(1999\)](#), who considered barotropic eddies near bottom bumps and seamounts, the latter idealized as right cylindrical obstructions. In Stern's study, the eddies were shielded, implying either a core of uniform vorticity surrounded by a strip of opposite signed vorticity, or a collection of point vortices of mixed sign, such that the net vorticity vanished. This constraint on the vorticity distribution ensures that the eddy has finite energy and also permits the vortices to move into a near-field interaction, as observed, with the topography. Stern demonstrated that such interactions could force a segregation of the centers of vorticity and thereby generate a dipole moment. Such moments can impart a stable self-propagation mechanism to vortices, as demonstrated in [Stern and Radko \(1998\)](#), and therefore topographic encounters were suggested for their role in influencing vortex dynamics. The paper ended with Stern generalizing his vorticity centroid invariance theorem to a two-layer quasigeostrophic system and speculating on vortex scattering scenarios for stratified fluids.

The significance of dipole moment generation is that of the possible inputs to vortex motion, that is, the  $\beta$  effect, mean flow advection, and self-propagation, the latter is emerging as perhaps the most oceanographically relevant. Radko (2000, manuscript submitted to *Rec. Adv. Phys. Oceanogr.*, hereafter RAD) provides a concise review. Stern's results provide an apparently robust mechanism for the generation of self-propagation tendencies (albeit in a barotropic setting), while allowing a vortex to retain a dominantly radial structure in keeping with observations. A separate mechanism relying on vortex instability has been proposed by [Morel and McWilliams \(1997\)](#).

*b. This paper*

The above papers, particularly [Stern \(1999\)](#), are built upon by considering the interactions of baroclinic vortices with topography. Stern's centroid theorem is first generalized to continuously stratified quasigeostrophic fluids. Additional assumptions are necessary to prove potential vorticity centroid conservation, which generalize the concept of an isolated vortex. These assumptions, however, are not required to prove the invariance of the dynamically important barotropic vorticity centroid. Next, vortex–bump interaction is examined in a two-layer fluid using point vortex and finite-difference models. This section addresses, among other things, whether weak lower-layer vorticity anomalies can impart measurable tendencies on strong upper layer vortices, and thereby control vortex propagation. It is argued topographic interactions have a pronounced tendency to scatter eddies into stable, generalized hetons (see [Hogg and Stommel 1987](#)) in geophysically relevant parameter regimes. Last, these calculations are extended to the case of finite-amplitude topography, where whole column cylinders in the presence of baroclinic point vortices are considered. Strong and weak interaction experiments support the above scattering tendency for this case. Accordingly, it is argued that baroclinic vortex propagation mechanisms are sensitive to vortex–topography interaction by means of scattering. The vortex–vortex self-propagation so induced is of the heton class, rather than the modon class as occurs in the barotropic case.

The next section describes the continuously stratified theorem. [Section 3](#) follows with the two-layer calculation and results. [Section 4](#) describes multilayer experiments with idealized seamounts, and the paper ends with a discussion section. Appendices contain some mathematical details and a description of the numerical procedure used to compute the Green's function for the point vortex in the presence of cylindrical seamounts.

## 2. Isolated vortices in continuously stratified fluids

The quasigeostrophic (QG) equation for a continuously stratified fluid on an  $f$  plane is

$$q_t + J(\psi, q) = 0; \quad q = \nabla_h^2 \psi + \frac{\partial}{\partial z} \frac{f_o^2}{N^2} \frac{\partial}{\partial z} \psi, \quad (1)$$

where  $\psi$  is a streamfunction and  $q$  is the potential vorticity of the fluid. The notation  $\nabla_h^2$  stands for the Laplacian operator in the horizontal,  $f_o$  is the Coriolis parameter, and  $N^2$  is the buoyancy frequency. The  $J$  denotes the usual Jacobian operator. To this equation are appended the boundary conditions

$$\psi_{zt} + J(\psi, \psi_z) = 0 \quad \text{at } z = 0, -H, \quad (2)$$

where  $H$  is the nominal depth of the fluid. Note that a flat bottom has been assumed.

To obtain a constraint on the potential vorticity center of mass, (1) is multiplied by the vector  $\mathbf{r}$ , denoting horizontal location, and volume integrated. It is simple to show that the integral of the weighted Jacobian vanishes, given that the present potential vorticity anomalies lie entirely within a finite volume. Thus,

$$\begin{aligned} & \frac{\partial}{\partial t} \int \int_{-\infty}^{\infty} \int_{-H}^0 \mathbf{r} q \, dV \\ & + \int \int_{-\infty}^{\infty} \int_{-H}^0 (\psi_y, -\psi_x) q \, dV = 0. \end{aligned} \quad (3)$$

Integrating the second term on the left by parts and applying (2) eventually yields

$$\begin{aligned} & \frac{\partial}{\partial t} \int \int_{-\infty}^{\infty} \int_{-H}^0 \mathbf{r} q \, dV \\ & = \left[ \int \int_{-\infty}^{\infty} (-\psi_y, \psi_x) \frac{f_o^2}{N^2} \psi_z \, dA \right]_{-H}^0. \end{aligned} \quad (4)$$

The comparable two-layer constraint derived by [Stern \(1999\)](#) is

$$\frac{\partial}{\partial t} \int \int_{-\infty}^{\infty} (H_1 q_1 + H_2 q_2) \mathbf{r} \, dA = 0, \quad (5)$$

where  $H_i$  and  $q_i$  are the layer thicknesses and potential vorticities respectively. [Equation \(5\)](#) shows there is a difference in the center of potential vorticity mass evolution between these two cases, reflecting buoyancy on the boundary. Movements

of nontrivial boundary buoyancy can shift the  $q$  centroid essentially by a vortex stretching mechanism. Such effects are avoided in the layered model by construction. Conservation of the  $q$  centroid for the continuously stratified case can be guaranteed if there is no buoyancy structure on the boundaries in the initial condition. [Equation \(2\)](#) then shows no such structure can develop on the boundaries and the right side contribution to [\(4\)](#) vanishes for all time. These are constraints in addition to those normally associated with an isolated vortex.

On the other hand, for the barotropic problem, the important dynamical constraint is on the vorticity centroid rather than the potential vorticity centroid. This was also the case for the two-layer theorem in [Stern \(1999\)](#), as [\(5\)](#) immediately yields

$$\begin{aligned} \frac{\partial}{\partial t} \iint_{-\infty}^{\infty} (H_1 q_1 + H_2 q_2) \mathbf{r} \, dA \\ = \frac{\partial}{\partial t} \iint_{-\infty}^{\infty} (H_1 \nabla^2 \psi_1 + H_2 \nabla^2 \psi_2) \mathbf{r} \, dA = 0, \end{aligned} \quad (6)$$

thus constraining the vertically integrated center of vorticity in a two-layer fluid.

If the vertical integration of the vortex stretching contribution to potential vorticity is explicitly carried out in [\(4\)](#) and [\(2\)](#), multiplied by  $\mathbf{r}$ , and area integrated, it is seen that

$$\frac{\partial}{\partial t} \iint_{-\infty}^{\infty} \int_{-H}^0 \nabla^2 \psi \mathbf{r} \, dV = 0. \quad (7)$$

Hence, the conservation of the vorticity centroid (usually defined as the dipole moment) for a continuously stratified quasigeostrophic fluid, *in the absence of external forces*, is proven.

To illustrate the ramifications of [\(7\)](#), consider a two-layer fluid with uniform potential vorticity patches in the upper and lower layers, surrounded by fluid of vanishing potential vorticity anomaly. It is further assumed that the bulk integrated potential vorticity vanishes; that is,

$$H_1 q_1 A_1 + H_2 q_2 A_2 = 0, \quad (8)$$

where  $A_i$  is the area of the vortex in layer  $i$  and  $q_i$  is the associated potential vorticity anomaly. [Equation \(5\)](#) can be evaluated in this case and is

$$\frac{\partial}{\partial t} (\bar{x}_1 - \bar{x}_2) q_1 A_1 H_1 = 0, \quad (9)$$

where  $\bar{x}_1$  and  $\bar{x}_2$  are the zonal centers of mass for the upper and lower vortices, respectively, and it is assumed the meridional centers of mass both vanish. [Equation \(9\)](#) demonstrates the ‘‘dipole moment’’ of this baroclinic vortex is conserved in the absence of external forces.<sup>1</sup>

If Green's theorem is now used, the propagation tendency of the upper-layer vortex center can be computed. For small separations, the formula is

$$\psi_{1x}(0, 0) = \frac{H_2 q_2 \bar{x}_2}{2H} \left[ -1 + \frac{a}{R} K_1 \left( \frac{a}{R} \right) \right], \quad (10)$$

where the vortices are both assumed circular, the upper vortex is centered at  $(0, 0)$ ,  $R =$

$$\frac{g' H_1 H_2}{(H_1 + H_2) f_o^2}$$

is the deformation radius, and  $a$  is the radius of the lower-layer patch (see [appendix A](#) for details). [Equation \(10\)](#) is related to a formula for slightly asymmetric barotropic eddy propagation appearing in [Stern \(1999\)](#) and can be used to estimate baroclinic eddy propagation.<sup>2</sup> Considering the interesting case of a weak lower-layer vortex under a strong upper-layer anticyclone,  $q_2$  is chosen as  $q_2 = 3 \times 10^{-6} \text{ s}^{-1}$  and  $H_2 = 3000 \text{ m}$ . If the upper layer is characterized by  $q = -3 \times 10^{-5}$  and  $H_1 = 1000$ , as suggested by [Schultz-Tokos and Rossby \(1991\)](#), the upper-layer signal is an order of magnitude greater than in the lower layer. The propagation speed of the upper center of mass is

$$v \approx \frac{H_2 q_2 \bar{x}_2}{H_1 + H_2} \approx 0.01 \text{ m s}^{-1} \quad (11)$$

for a separation of 20 km, which compares well to the observed meddy speeds of  $0.02 \text{ m s}^{-1}$ . Given the smallness of this distance and the weakness of the lower-layer potential vorticity anomaly, direct observation of the lower-layer vortex would be demanding. The velocity field surrounding meddies is not well known because most meddy observational programs have focused on the meddies themselves. There is also lack of deep observations under meddies, again because the observational focus, particularly with floats, has concentrated on typical meddy central depths. In any case, there is little to no evidence of coherent deep circulations associated with meddies, a feature reflected in the present model by the weak deep flows assumed in (11). Yet, in determining the overall propagation speed of the vortex, such flows would be dominant. Thus it is plausible to consider this self-propagation mechanism as an explanation of meddy propagation speeds *provided vortex configurations can be found that are stable and at most slowly varying*.

The theorem in (7) and the accompanying discussion provide the backdrop for the following numerical experiments. A geophysically relevant question, given the observations, is if weak vorticity anomalies under surface intensified eddies will impact their propagation as the eddies drift over topography. Such interactions appear inevitable and represent conditions breaking the assumptions built into both (6) and (7). Dipole moments will generally not be indefinitely preserved, and the question becomes what types of vortex structures emerge from these interactions. Does the concept of a dipole moment and its associated propagation influence play a useful role in explaining subsequent eddy evolution and, if so, what speeds are involved? Are such moments stable? These questions are considered in the next sections.

### 3. Baroclinic vortices near bumps

Consider a vortex in a two-layer  $f$  plane fluid impinging on a bump. The QG equations governing this encounter are

$$q_{it} + J(\psi_i, q_i) = F_i - C_d \nabla^2 \psi_2 \hat{\delta}_{i,2}, \quad i = 1, 2, \quad (12)$$

where

$$q_i = \nabla^2 \psi_i + (-1)^i f_o \frac{h_1}{H_i} + f_o \frac{h_b}{H_2} \hat{\delta}_{i,2} \quad (13)$$

defines layer potential vorticity,  $i$  is the layer index, and  $F_i$  denotes friction in the  $i$ th layer. Biharmonic friction will be used for  $F_i$  in all experiments shown here. The quantity  $h_1$  is defined by  $f_o(\psi_1 - \psi_2)/g'$ , where  $g'$  is the reduced gravity of the interface. The quantity  $\hat{\delta}_{i,2}$  denotes the Kronecker delta function and  $C_d$  denotes a bottom drag coefficient.

#### a. Point vortex calculations

The neglect of  $\beta$  in (12) can be rationalized in a couple of ways given meddy and SCV parameters. First, meddies are characterized by radii of 25–50 km and swirl speeds in excess of  $0.2\text{--}0.3 \text{ m s}^{-1}$ . These yield Rossby numbers (Ro) of 0.2 (see also [Schultz-Tokos and Rossby 1991](#)). The importance of  $\beta$  is relatively weak, as expressed by the ratio of the  $\beta$  contribution to potential vorticity to that from relative vorticity

$$\frac{\beta y}{\nabla^2 \psi} \approx \frac{\beta y}{f_o \text{Ro}} \approx \frac{2 \times 10^{-11} (\text{ms})^{-1} 10^5 \text{ m}}{10^{-4} \text{ s}^{-1} 0.2} = 0.1. \quad (14)$$

Second, it is useful to compare the observed meddy propagation rates of  $0.02 \text{ m s}^{-1}$  to that expected from the  $\beta$  effect. The latter is estimated by [Nof \(1982\)](#) to be  $O(0.001 \text{ m s}^{-1})$ , suggesting that non- $\beta$  propagation mechanisms must play a role. These we will study using point vortex techniques.

Topography in this problem is confined to the lower layer and all frictional parameters are neglected. In this case, potential vorticity is a conserved quantity, a point exploited by writing it in layer  $i$  as

$$q_i = \sum_j a_{ij} \delta(\mathbf{r} - \mathbf{r}_{ij}), \quad (15)$$

where  $\delta$  is the Dirac delta function. Identifying meddies with patches of anomalous potential vorticity is also consistent with their probable formation, involving entrainment of background Atlantic water by boundary currents of pure Mediterranean outflow. Note that (15) implies potential vorticity vanishes everywhere away from the point vortices, even over the bump. Such a situation will arise under suitable initial conditions, or under arbitrary initial conditions if all of the fluid initially over the bump is swept downstream. Manipulation of (13) yields the equations

$$\nabla^2 \psi_c - R^{-2} \psi_c = f_o \frac{h_b}{H_2} + q_1 - q_2 = f_o \frac{h_b}{H_2} + q_c$$

$$\begin{aligned} \nabla^2 \psi_b &= -f_o h_b + H_1 q_1 + H_2 q_2 \\ &= -f_o h_b + q_b \end{aligned} \quad (16)$$

governing the horizontal structure associated with the vertical normal modes  $\psi_b$  and  $\psi_c$ , where  $\psi_b = H_1 \psi_1 + H_2 \psi_2$  and  $\psi_c = \psi_1 - \psi_2$ . The quantities  $q_c = q_1 - q_2$ , and  $q_b = H_1 q_1 + H_2 q_2$  are the potential vorticity projections of the two-layer system onto the barotropic and baroclinic modes. The quantity  $R$  is the first deformation radius

$$R^2 = g' \frac{H_1 H_2}{(H_1 + H_2) f_o^2}$$

Isolated, radially symmetric topography centered at  $\mathbf{r} = 0$  is considered, implying  $h_b = 0$  for  $|\mathbf{r}| > r_o$ . The assumption that potential vorticity vanishes aside from point vortices requires that we further impose

$$\int_0^{r_o} \rho h_b(\rho) d\rho = 0 \quad (17)$$

to insure the circulation bound to the topography has finite energy [this is easily shown from (16)].

The linearity of (16) permits  $\psi_b$  and  $\psi_c$  to be broken into three pieces: one for the point vortices, one for the topography, and one for the mean flow. In this case, the solutions of (16), including a barotropic mean flow, are

$$\begin{aligned} \psi_c &= -\sum_{i=1}^2 \sum_{j=1}^{nv(i)} \frac{(-1)^{(i+1)} a_{ij} K_o(|\mathbf{r} - \mathbf{r}_{ij}|/R)}{2\pi} + AK_o\left(\frac{|\mathbf{r}|}{R}\right) \\ \psi_b &= \sum_{i=1}^2 \sum_{j=1}^{nv(i)} \frac{H_i a_{ij} \ln(|\mathbf{r} - \mathbf{r}_{ij}|)}{2\pi} - U_o H y, \end{aligned} \quad (18)$$

where  $H = H_1 + H_2$ , for  $|\mathbf{r}| > r_o$ . The constant  $A$  in the above is given by

$$A = \frac{-R \int_0^{r_o} \hat{r} I_o\left(\frac{\hat{r}}{R}\right) \frac{f_o h_b}{H_2} d\hat{r}}{r_o \left[ K_o\left(\frac{r_o}{R}\right) I_1\left(\frac{r_o}{R}\right) + K_1\left(\frac{r_o}{R}\right) I_o\left(\frac{r_o}{R}\right) \right]}. \quad (19)$$

Equation (17) implies that the bump generates no barotropic circulation; an example of a bump satisfying this constraint is a hill surrounded by a weak valley. Such topography still generally supports a bound vortex with a baroclinic expression outside  $r_o$ . The bottom circulation at the edge of a 100-m-tall cosine-shaped bottom bump of radius 35 km, as computed using (19), is about  $0.002 \text{ m s}^{-1}$ . Equations (18) yield the layer pressures, namely,

$$\psi_1 = (H_2 \psi_c + \psi_b)/H; \quad \psi_2 = (\psi_b - H_1 \psi_c)/H \quad (20)$$

from which velocities may be deduced by geostrophy. The vortices are then advected and used to reevaluate the layer streamfunctions according to (18) and (20).

Figure 2 shows typical results from experiments of this type. The vortex in this case consisted of two point vortices of equal, but opposite strength in layers of 500 m thickness. They were situated one over the other and started at a distance of 500 km east of the bump. A barotropic mean flow of  $0.02 \text{ m s}^{-1}$  advected them into a near-field interaction with the topography. Their position relative to the bump center was varied and results from four such experiments are shown. The meridional initial positions of these vortices were 20, 10, -10, and -20 km relative to the center of the bump.

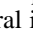
The upper panel contains the trajectories of the upper vortex of the pair (the lower vortex trajectories were in all these


cases essentially indistinguishable from that shown). Upstream of the bump, the trajectories are consistent with the advection field. In all cases, however, the interaction with the topography generates curvature in the trajectory, followed by propagation at a new steady rate. The lower panel shows a typical time history of the separation of the point vortices from the experiment indicated by the arrow in the upper panel. The early stages are characterized by the two members moving as a unit. This is followed by a fairly complex trajectory in the immediate vicinity of the bump, during which time the pair separates. The subsequent trajectory quickly falls into an equilibrium characterized by a fixed separation. Note that the separation occurs in both east–west and north–south directions, with the stronger of the two being the zonal. This separation also gives rise to the new vortex propagation tendencies in the direction normal to the advecting current. In this case, the relative speed is roughly  $0.01 \text{ m s}^{-1}$ , comparable to that of the advective velocity itself.




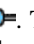
These experiments address the issue of the influence of the bottom topography on a vortex. Specifically in “weak”<sup>3</sup> interactions such as these, the vortex can scatter from the topography at an angle driven by the topographically induced tendency for the vorticity centroid to evolve.


### b. Continuous vortices


Several point vortex experiments were run, all yielding results essentially like those described above. Experimentation with a finite-difference QG numerical model, set in a periodic channel, was then pursued to investigate continuous vorticity patches.

The parameters used typically consisted of  $H_1 = 1000 \text{ m}$ ,  $H_2 = 3000 \text{ m}$ ,  $f_o = 10^{-4} \text{ s}^{-1}$ ,  $\kappa = -3 \times 10^8 \text{ m}^4 \text{ s}^{-1}$ , and  $C^{-1}_d = 1000 \text{ days}$ . Slip boundary conditions were employed and Gaussian bottom topographies of variable height and radius were used. Several initial vortex structures and barotropic advection speeds were examined. [Figure 3](#)  contains the results of an experiment with a 400 m Gaussian bump, an  $e$ -folding scale of 30 km and a barotropic advection of  $-0.02 \text{ m s}^{-1}$ . The initial upper-layer potential vorticity distribution was taken to be constant at  $-0.3 f_o$  inside of 30 km (the deformation radius was 48 km) in the upper layer. [Even though the implied Rossby number in these experiments (0.3) is not small, experience with quasigeostrophic models suggests that they display qualitatively useful evolution in this range. This is partly due to the conservation of potential vorticity that governs strong vortices such as meddies.] The lower-layer potential vorticity anomaly was also constant, but extended to 60 km. The requirement of no net barotropic potential vorticity anomaly was enforced, making the lower vorticity anomaly roughly an order of magnitude weaker than that of the upper layer. The lateral vortex structure was composed of Bessel functions and logarithms, as required by the solution of (16) for uniform vorticity and a flat bottom. The vortex center was initially placed 200 km south and 350 km east of the topographic center.

[Figure 3](#)  shows a composite diagram of the upper-layer potential vorticity for times before and after the topographic interaction. The upper panel contains the upper-layer  $q$  anomaly and the lower panel the bottom-layer  $q$  anomaly. The location of the topography is indicated in both plots and a persistent, nearly steady anticyclonic circulation appears in the lower layer over the bump. Note that the coherence of the vortex structure has survived in both layers, placing this in the weak interaction category. Considerable distortion of the lower  $q$  field has occurred, but the later distorted structure is stable, as evidenced by the intermediate and later times. It is also evident that the vortex in the later time period is moving southward. This later period is also characterized by a considerable separation from the bump, arguing that the vortex motion is now independent of any direct topographic effect. Further evidence of this is that the bump circulation field is anticyclonic, as seen in the lower-layer  $q$  plots, and would induce a northward drift on the vortex as contrasted to the observed southward motion.

[Figure 4](#)  shows a composite of the upper- and lower-layer potential vorticities at two later dates from [Fig. 3](#) , from which it is clear that the vortex is a coherent structure including the lower layer. The initial structure of this vortex was radially symmetric with the centers of the potential vorticity anomalies in each layer aligned vertically. By the latter date, the upper- and lower-layer centers have separated, giving rise to a dipole moment à la (7). This configuration is called “hetonlike,” after the original heton formulation first found by [Hogg and Stommel \(1987\)](#). On the other hand, the overall structure of the upper layer, which is where the dominant kinematic and dynamic signature of the vortex is found, is still circularly symmetric. The layer vortex centers are arranged with the lower cyclone to the east of the upper anticyclone, a configuration set to generate southward propagation as observed. The vortex meridional center of mass location as a function of time is plotted in [Fig. 5](#) , demonstrating a southward propagation of roughly  $0.01 \text{ m s}^{-1}$ . The zonal center of mass trajectory appears in [Fig. 6](#) . The later zonal speeds are slower than  $0.02 \text{ m s}^{-1}$  to the west due to the eastward-directed self-propagation of the induced heton.

An example of a “strong” interaction between a baroclinic vortex and topography appears in [Fig. 7](#) . This is a composite of three snapshots of the  $q$  anomalies (the bump location is indicated). The distinction between this and the previous experiment is that the association between the upper and lower layers is undermined. The two vortices are stripped apart and, as shown principally by the upper vortex trajectory, subsequently are carried zonally by the advecting current. It is interesting that the separate centers maintain their coherent structures throughout the sequence.

While the upper-layer survival appears to be robust for a variety of initial states, the lower layer can exhibit more complex behaviors. [Figure 8](#)  shows a composite of the lower-layer evolution during a very strong interaction. Not only are the upper and lower layers stripped apart, but the lower layer is sheared out to a zonal tendril. The survival of the upper-layer vortex is perhaps not surprising given that the topography directly affects only the lower layer.

Bottom irregularities are common, although diverse in structure and amplitude. The effect of a distributed set of bottom bumps can be considered by examining (16) in the presence of a large number topographic centers at random locations and of random amplitudes. Examples of the trajectories so computed are compared in Fig. 9, where the three pathways shown are differentiated by their initial conditions being 5 and 10 km apart. In all cases, the vortices were subject to a far-field westward barotropic mean flow of  $0.02 \text{ m s}^{-1}$ . Trajectories of both the upper and lower vortex centers are shown in the plot to emphasize that they track each other. The topography in this case consisted of 200 bottom bumps distributed randomly over an area of  $2000 \text{ km} \times 2000 \text{ km}$ . This yields an average separation of 140 km, not unlike the major topographic anomalies seen in Fig. 1. The amplitude of the bumps was taken from a Gaussian distribution centered on 100 m and with  $e$ -folding scale of 50 m. (Negative heights generated by the random number sequence were simply converted to positive values.) The lateral scale of the bottom bumps was taken to be the 35-km deformation radius. Such bumps are characterized at a distance of one deformation radius from their centers roughly by an anticyclonic deep circulation of  $3 \times 10^{-3} \text{ m s}^{-1}$ .

The motivation for showing Fig. 9 here is because meddy trajectories are observed to be irregular. This feature was one of the main observational aspects of meddies, to which Morel and McWilliams (1997) appealed to support the applicability of their unstable meddy model. Clearly, a similar highly time-dependent nature can be imparted to meddy and SCV trajectories by their interactions with distributed bottom topography.

#### 4. Vortex interactions with strong topography

The previous calculations involved topography that is small in the usual QG sense. On the other hand, meddies and vortices in general are likely to encounter seamounts as well as bumps on the bottom. It is not possible to categorize such topography as small; rather, a much more intuitively satisfactory idealized model of seamounts is as a cylinder extending through the entire water column. Meddy–seamount interaction is examined in the present section using a point vortex approach, whereby the vortex is modeled as a cloud of point vortices embedded in a three-layer fluid. The net barotropic potential vorticity anomaly vanishes here due to the presence of opposite signed  $q$  anomalies in the various layers.

Three layers, rather than two, are chosen because meddies are vortices embedded in the thermocline. This feature can be captured by placing the potential vorticity anomaly in the middle layer. The three-layer model is also dynamically richer than the two-layer case because of the presence of a second deformation radius. Finally, comparisons of some of the upcoming results with observations will be given later, an activity that the more “realistic” three-layer model facilitates.

One important distinction between this configuration and that of the weak bumps is that the perturbations to the mean flow induced by the topography are different. Note that in the weak topography formulation, circulations form over the bump because of vortex stretching. Such compression is not possible for seamounts extending throughout the column. Instead, the flow parts around the seamounts with a degree of asymmetry caused by the presence of other seamounts in the neighborhood.

A point vortex approach is used because the presence of a circular boundary is relatively straightforward to include. In contrast, in a classical gridpoint formulation, the seamount boundary would entail a series of steps on which no-normal-flow boundary conditions would apply. These have the potential to make the boundary interaction very viscous. On the other hand, the inviscid problem seems more relevant because vortex–seamount interactions, inasmuch as they have been observed for meddies, are short-lived events. It is therefore questionable if the potential vorticity anomaly of the vortex can be significantly modified during the encounter. (It is also possible to employ boundary-fitted coordinates to handle the seamount. These would remove the finite-difference concerns mentioned above, but such a model has not been developed here.)

Contour dynamics (Stern and Pratt 1985) methods also lend themselves to this problem, but have not been used in order to avoid the contour surgery that would be required if the vortices “broke” around the seamount. Nonetheless, the calculation of Green's function for this problem is a computationally challenging task and is described in appendix B. For present purposes, it is noted that the employed procedure is iterative and can accommodate any number of layers (the specific case of three layers is demonstrated in appendix B), vortices or seamounts, and any size and location for the seamounts. All seamounts are, however, restricted to circular symmetry.

Radially symmetric vortices are used at the outset and are brought into the near field of the seamounts by means of a barotropic flow. At large distance, this flow is uniform at values of  $-0.02 \text{ m s}^{-1}$ .

An example of vortex–seamount interaction appears in Fig. 10, where before and after states are shown. This vortex began at (150 km, 0 km), moving westward into an interaction with a seamount located at (0, 90 km). The seamount radius was 50 km. The uppermost of the three layers was 100 m thick, the second 300 m, and the third 3000 m. No point vortices were introduced into the first layer. The second layer housed a vortex of 30-km radius and a Rossby number of  $-0.2$ . The third layer included a vortex of the same radius and a Rossby number of 0.02, that is, 10 times smaller than that of the upper layer. The initial radially symmetric configuration appearing in the figure maintained itself for roughly 100 days prior to the interaction with the seamount. The configuration would be stable in the absence of external effects for the duration of the experiment. The distortion experienced by the vortex due to the seamount encounter is clearly minor, as also seen in the



figure. The main effect is in the separation of the vorticity centers of the two layers. The subsequent trajectory of this newly developed generalized hetonlike pair included a persistent northward drift at the rate of  $0.01 \text{ m s}^{-1}$ . Once formed, this latter configuration was also apparently stable and persisted for several hundred more days.

The vortex center separation of the upper and lower layer vortices is documented in [Fig. 11](#), where the zonal and meridional  $q$  center history from this vortex is shown. The first part of the history is dominated by the two centers tracking each other, as expected from their radial symmetry and overall stability. As they move into the seamount encounter, the separations exhibit a reasonably complicated pattern, characterized by time-dependent separations in the zonal and meridional directions. These settle to finite values as the vortex exits the seamount neighborhood, with the zonal separation being the largest. This separation is the one responsible for the northward migration. Note however, that the meridional separation is arrayed so as to impede the westward vortex advection by the barotropic flow. The zonal speed of the vortex self-propagation is roughly  $0.005 \text{ m s}^{-1}$ , representing a measurable slowing of the vortex.

Several initial value experiments of this sort were conducted, each differentiated from the others by the initial vortex placement relative to the seamount with all other parameters remaining unchanged. The initial point vortex centers were positioned 200 km east of the seamount and at points 120, 90,  $-90$ ,  $-100$ , and  $-120$  km north of the seamount center. The seamount itself had a radius of 50 km. The vorticity center trajectories over a period of 200 days from these cases are shown in [Fig. 12](#). Note that, depending on the nature of the interaction, both northward and southward self-propagations can develop. Also the zonal self-propagation generated by the interaction can be in either sense. This appears in the trajectories south of the seamount zonally lagging those north of the seamount. These lags are caused by the vortices to the south developing an eastward self-propagation tendency, while those to the north develop a westward tendency and reinforce the advection.

An example of a strong interaction with strong topography is shown in [Fig. 13](#). In this case, the vortex initial location was at (150 km, 0 km) while the cylinder was at (0 km, 30 km). The subsequent evolution differed markedly from the weak interaction scenario. Rather than directly scattering into a hetonlike configuration, the vortex broke around the seamount. (Note, the breaking does not involve direct contact of the meddy with the topography.) This involved the upper and lower centers moving largely in opposite senses about the seamount, as seen in [Fig. 13](#). These are very complicated histories, and are under further study; nonetheless, the subsequent evolution shows an unexpected tendency to reorganize into a hetonlike configuration. The interaction of the centers after their topographic separation is mediated by the seamount geometry. Given their split, it is essentially impossible for the upper and lower  $q$  anomalies to reunite in a radially symmetric shape; therefore, the resultant structure is dipolar. The subsequent center displacement generates a dipole moment whose interaction drives the vortex away from the topography.

Note the later heton formation is not a perfect process. Some of the initial vortex mass is lost from the emerging heton. This experiment, however, shows that a majority of the mass can reorganize into a coherent vortex. This is a result typical of several such experiments, suggesting heton generation is a very robust vortex mechanism.

It is interesting to comment on the similarities between this experiment and the observations, [Shapiro et al. \(1995\)](#), of the structure of a meddy that had recently encountered a seamount. They reported that Meddy Irving partially survived its interaction with the Irving Seamount, emerging as a coherent eddy. Further, they found a wake of saline water trailing the meddy, apparently made of diluted water from the vortex periphery and two smaller cores of much more pure vortex stock. These features appear in the above experiment. Namely, the vortex survives as a coherent structure in spite of a very strong topographic encounter. A wake of vortex water is generated however, appearing in [Fig. 13](#), as the point vortices detached from and trailing the main dipole. A few smaller cores of more intense  $q$  anomaly appear in the wake. Since a Lagrangian problem is solved to determine the evolution of this system, the distribution and density of point vortices can equally well be interpreted in terms of salinity or potential temperature, a view that strongly connects this experiment with the Irving data. Of the 81 point vortices initially in the meddy, approximately 23, or 28% of the total, are expelled. [Shapiro et al. \(1995\)](#) report somewhere between 20% and 27% of the buoyancy anomaly of Meddy Irving was found in its wake. The experiment rationalizes those data and their interpretation in terms of potential vorticity dynamics. The survival of the meddy is ascribed to the persistence of the  $q$  anomaly and the strong tendencies of anomalies to regularize.

## 5. Discussion

The problem of vortex topography interaction has been studied with particular, but not sole, emphasis on weak interactions, where the integrity of the vortex prior to interaction is largely maintained throughout the interaction. This is a problem motivated by the apparent ubiquity of subsurface coherent vortices in the World Ocean along with the global distribution of nontrivial bottom topography. Baroclinic vortices are studied, both as a complement to the earlier work on barotropic vortices conducted by [Stern \(1999\)](#) and because of the large numbers of observations of baroclinic vortices in the ocean.

The most well-observed member of the subsurface vortex class is the meddy, and an unresolved issue surrounding them is the identification of the mechanisms responsible for their propagation. Evidence is provided here that topographic interactions can often induce dipole moments in baroclinic vortices and the generation of apparently stable hetonlike structures capable of effecting important vortex self propagation. Given the generic character of bottom irregularities, vortex trajectories so-influenced should be themselves irregular, and exhibit a number of kinks and turns. These are indeed both computed in the present case and observed in the ocean.

Many of the above results were argued based on point vortex calculations, but finite-difference models have also been used. The basic tendency for vortices to scatter into continuously distributed generalized hetons was found in this case as well. These structures were found to be very stable and capable of surviving during propagations over many eddy radii. This is significant as there are few examples of hetons with continuous potential vorticity distributions.

Both small topography and seamounts have been considered as limiting examples of topographic interactions. In both cases, scattering into a hetonlike configuration is typical, even though the nature of the interaction between the cases is quite different. Evidence is also offered that this is a very robust tendency, occurring even in instances where the vortex can break around the seamount. A correspondence has been found between the highly idealized experiments in this case and the observations of a meddy shortly after encountering topography. Those observations suggest that vortex–seamount interaction need not be fatal, and this is certainly consistent with the present results. Such interactions can “wound” the vortex however, and computed losses from the main coherent structure are quite like those estimated from data.

The existing meddy observational database does not make a strong case for counterrotating flows persistently in the vicinity of meddies. On the other hand, the cases studied here consist of vortices for which the cyclonic companions of the anticyclones are comparatively weak, and therefore would be challenging to identify in observations. They are also underneath the core anticyclone, where few observations exist, a shortcoming that future observational programs may wish to address.

Relative to the issue of weak asymmetry in vortices, one point is worth making explicit. RAD argues that vortices governed by reduced-gravity,  $f$ -plane, quasigeostrophic dynamics with weak asymmetries do not survive for long. A reason forwarded for this is that these equations require the center of mass to be motionless. Asymmetries initially present in vortex can cause vortex migration, but the vortex is nonetheless constrained not to wander far from its initial location as a coherent vortex. The asymmetries quickly break down, and a motionless symmetric structure occurs. Quasigeostrophic  $\beta$ -plane dynamics require the center of mass to move westward at the long-wave speed. While less experimental work has been done on the  $\beta$  plane, the mechanics of vortex regularization are still at work and it is plausible that reduced-gravity, weakly asymmetric eddies still survive only for propagations of several diameters. An unexpected result argued by RAD is that primitive equation  $f$  plane, reduced-gravity vortices with weak asymmetry are longer lived than  $f$ -plane QG eddies, an effect that he shows is due to gravity wave dynamics. These results suggest weak asymmetry can be difficult for vortices to sustain for long periods of time. The experiments here show very different characteristics. The weak asymmetry, at the heart of the vortex propagation, resides in different layers. This implies that vortex regularization is less likely to dominate, and the vortices at the outset break the reduced-gravity requirement. It appears that this combination of ingredients can result in stable and very long lived asymmetric configurations on the  $f$  plane that are capable of significant self-propagation. This feature perhaps suggests that the current model is more applicable to observed vortices than is the reduced-gravity model.

In summary, these results argue two conclusions: First, topographic interactions are an almost inevitable source of long-lived weak asymmetry in vortices and therefore of importance to vortex trajectories. The self-propagation tendencies so generated are comparable to those observed and the distribution of topography lends a random-looking component to vortex movement. Second, even strong interactions, during which the integrity of the vortex is severely disrupted, can fail to destroy the eddy. The eddy  $q$  anomalies are strong and survive the encounter. The subsequent evolution of the system is capable of reorganization. These results support the suggestion by [Shapiro et al. \(1995\)](#) that meddy–seamount interaction need not be fatal. It is interesting to speculate that vortices generally survive strong seamount interactions, with a concomitant and small loss of mass to the surrounding fluid. This conjecture is currently under study.

#### Acknowledgments

WKD is supported by NSF Grant ATM-9818628 and NASA Grants NAG5-7630 and NAG5-8291, the latter awarded in support of the NASA Seasonal to Interannual Prediction Project. The author wishes to acknowledge a number of interesting conversations with Melvin Stern and Gouhui Wang. Ms. J. Jimeian assisted with computational issues. This is a contribution of the Climate Institute, a Center of Excellence support by the Research Foundation of the Florida State University.

---

#### REFERENCES

- Armi L., D. Hebert, N. Oakey, J. Price, P. Richardson, H. Rossby, and B. Ruddick, 1989: Two years in the life of a Mediterranean salt lens. *J. Phys. Oceanogr.*, **19**, 354–370. [Find this article online](#)
- Carnevale G., R. Kloosterziel, and G. van Heijst, 1991: Propagation of barotropic vortices over topography in a rotating tank. *J. Fluid Mech.*, **233**, 119–139. [Find this article online](#)
- Ebbesmeyer C., B. Taft, J. McWilliams, C. Shen, S. Riser, T. Rossby, P. Biscay, and H. Ostlund, 1986: Detection, structure and origin of extreme anomalies in a western Atlantic oceanographic section. *J. Phys. Oceanogr.*, **16**, 591–612. [Find this article online](#)
- Hogg N., and H. Stommel, 1987: The heton: An elementary interaction between discrete baroclinic geostrophic vortices, and its implications concerning eddy heat-flow. *Proc. Roy. Soc. London*, **A397**, 1–20. [Find this article online](#)
- Louis J., and P. Smith, 1982: The development of the barotropic radiation field of an eddy on a slope. *J. Phys. Oceanogr.*, **12**, 56–73. [Find this article online](#)

McDowell S., and T. Rossby, 1978: Mediterranean Water: An intense mesoscale eddy off the Bahamas. *Science*, **202**, 1085–1087. [Find this article online](#)

McWilliams J., 1985: Submesoscale, coherent vortices in the ocean. *Rev. Geophys.*, **23**, 65–182. [Find this article online](#)

Morel Y., and J. McWilliams, 1997: Evolution of isolated interior vortices in the ocean. *J. Phys. Oceanogr.*, **27**, 727–748. [Find this article online](#)

Nof D., 1982: On the movements of deep mesoscale eddies in the North Atlantic. *J. Mar. Res.*, **40**, 57–74. [Find this article online](#)

Prater M., and T. Rossby, 1999: An alternative hypothesis for the origin of the “Mediterranean” salt lens observed off the Bahamas in the fall of 1976. *J. Phys. Oceanogr.*, **29**, 2103–2109. [Find this article online](#)

Richardson P., and A. Tychensky, 1998: Meddy trajectories in the Canary Basin measured during the SEMAPHORE experiment, 1993–1995. *J. Geophys. Res.*, **103C**, 25029–25045. [Find this article online](#)

Richardson P., A. Bower, and W. Zenk, 2000: A census of Meddies tracked by floats. *Progress in Oceanography*, Vol. 45, Pergamon, 209–250.

Schultz-Tokos K., and T. Rossby, 1991: Kinematics and dynamics of a Mediterranean salt lens. *J. Phys. Oceanogr.*, **21**, 879–892. [Find this article online](#)

Shapiro G., S. Meschanov, and M. Emelianov, 1995: Mediterranean lens “Irving” after its collision with seamounts. *Oceanol. Acta*, **18**, 309–318. [Find this article online](#)

Smith D., 1986: A numerical study of Loop Current eddy interaction with topography in the western Gulf of Mexico. *J. Phys. Oceanogr.*, **16**, 1260–1272. [Find this article online](#)

Stern M., 1999: Scattering of an eddy advected by a current towards a topographic obstacle. *J. Fluid Mech.*, **402**, 211–223. [Find this article online](#)

Stern M., and L. Pratt, 1985: Dynamics of vorticity fronts. *J. Fluid Mech.*, **161**, 513–532. [Find this article online](#)

Stern M., and T. Radko, 1998: The self-propagating quasi-monopolar vortex. *J. Phys. Oceanogr.*, **28**, 22–39. [Find this article online](#)

Weatherly G., M. Arhan, H. Mercier, and W. Smethie, 2002: Evidence of abyssal eddies in the Brazil basin. *J. Geophys. Res.*, in press.

Yasuda I., K. Okuda, and K. Mizuno, 1986: Numerical study on the vortices near boundaries—Considerations of warm core rings in the vicinity of the east coast of Japan. *Bull. Tohoku Reg. Fish. Res. Lab.*, **48**, 67–86.

---

## APPENDIX A

### 6. Center of Mass Velocity

Consider a two-layer, inviscid,  $f$ -plane, quasigeostrophic fluid and assume patches of uniform potential vorticity occur in each layer such that

$$q_1 H_1 A_1 + q_2 H_2 A_2 = 0,$$

where  $q_1$  and  $q_2$  are the layer potential vorticities,  $H_1$  and  $H_2$  are the layer thicknesses, and  $A_1$  and  $A_2$  are the areas of the patches. The solution to (16) is

$$\begin{aligned}\psi_b(\mathbf{x}_o) &= \iint G_b(\mathbf{x}_o; \mathbf{x}) q_b(\mathbf{x}) d\mathbf{x} \\ \psi_c(\mathbf{x}_o) &= \iint G_c(\mathbf{x}_o; \mathbf{x}) q_c(\mathbf{x}) d\mathbf{x},\end{aligned}\quad (\text{A1})$$

where the barotropic and baroclinic Green's functions are

$$G_b(\mathbf{x}_o; \mathbf{x}) = \frac{1}{2\pi} \ln(|\mathbf{x} - \mathbf{x}_o|). \quad (\text{A2})$$

Consider a two-vortex configuration where it is assumed that they occur one in each layer, the vortex boundaries are circular, and the upper and lower centers are found at  $(0, 0)$  and  $(x_2, 0)$ , respectively. Using standard contour dynamics manipulations, the contribution to the meridional velocity at the upper vortex center by the baroclinic mode  $\psi_c$  is given by

$$\psi_c(0, 0) = \frac{q_2}{2\pi} \oint K_o\left(\frac{|\mathbf{x}|}{R}\right) \hat{i} \cdot \mathbf{n} dl, \quad (\text{A3})$$

where the outward pointing unit normal vector of the layer-two vortex is denoted by  $\mathbf{n}$ . A similar formula yields the barotropic contribution at this same point. Assuming the separation of the two centers is small compared to the deformation radius, the argument of the integral in (A3) can be Taylor expanded, and the integral evaluated. Following a similar procedure for the barotropic mode and then computing the upper-layer velocity according to (20) yields (10).

## APPENDIX B

### 7. A Point Vortex Model of Meddy–Seamount Interaction

The inviscid, three-layer, unforced, layered quasigeostrophic (QG) equations on an  $f$  plane are

$$\frac{d}{dt} q_i = 0, \quad i = 1, 2, 3$$

in which

$$\begin{aligned} q_1 &= \nabla^2 \psi_1 - f_o^2 \frac{\psi_1 - \psi_2}{g'H_1} \\ q_2 &= \nabla^2 \psi_2 + f_o^2 \frac{\psi_1 - \psi_2}{g'H_2} - f_o^2 \frac{\psi_2 - \psi_3}{g''H_2} \\ q_3 &= \nabla^2 \psi_3 + f_o^2 \frac{\psi_2 - \psi_3}{g''H_3}, \end{aligned} \quad (\text{B1})$$

where  $f_o$  denotes the Coriolis parameter,  $H_i$  the average thickness of layer  $i$ ,  $\psi_i$  the  $i$ th layer streamfunction,  $d/dt$  the quasigeostrophic material time derivative

$$\frac{d}{dt} = \frac{\partial}{\partial t} + J(\psi_i, \cdot),$$

and  $g', g''$  the reduced gravities of the two interfaces. A solution to (B1) under these constraints is

$$q_i(\mathbf{x}, t) = q_i(\mathbf{x}_o, 0); \quad \mathbf{x} = \mathbf{x}_o + \int_o^t \mathbf{u}(\mathbf{x}, t) dt, \quad (\text{B2})$$

expressing the conservation of potential vorticity by fluid parcels.

Consider now a patch of anomalous potential vorticity on an  $f$  plane, embedded within a fluid of otherwise vanishing potential vorticity and threaded vertically at NC locations,  $\mathbf{r}_k$ , by solid circular islands of radius  $a_k$ . The boundary conditions for this system are  $\psi_i \rightarrow f(\mathbf{r})$  for  $\mathbf{r} \rightarrow \infty$  where  $f(\mathbf{r})$  is the known undisturbed far-field flow, no-normal flow on the cylinder boundaries  $\psi_i(\mathbf{r}_k + a_k \hat{\mathbf{r}}_k) = c_k = \text{constant}$ , where  $\hat{\mathbf{r}}_k$  denotes the radial unit vector centered at  $\mathbf{r}_k$  and

$$\oint_0^{2\pi} \psi_r a_k d\theta = S_k = 0, \quad (\text{B3})$$

stating the persistence of the circulation,  $S_k$ , around an island.

Defining

$$\gamma_{\pm} = -\frac{g'}{2g''} \left\{ \frac{H_2 + H_3}{H_3} - \frac{g''(H_1 + H_2)}{g'H_1} \pm \left[ \left( \frac{H_2 + H_3}{H_3} - \frac{g''(H_1 + H_2)}{g'H_1} \right)^2 + \frac{4g''}{g'} \right]^{1/2} \right\}, \quad (\text{B4})$$

*(Click the equation graphic to enlarge/reduce size)*

the layer potential vorticity equations can be written as

$$\nabla^2 \psi_b = q_b, \quad \nabla^2 h_{\pm} - R_{\pm}^{-2} h_{\pm} = q_{\pm}, \quad (\text{B5})$$

where

$$h_{\pm} = f_o \left( \frac{\psi_1 - \psi_2}{g'} + \gamma_{\pm} \frac{\psi_2 - \psi_3}{g''} \right) = h_1 + \gamma_{\pm} h_2$$

$$q_{\pm} = \frac{f_o}{g'} [q_1 + (\gamma_{\pm} - 1)q_2 - \gamma_{\pm} q_3]$$

$$R_{\pm}^2 = \frac{g'H_2H_1}{f_o^2(H_1 + H_2 - \gamma_{\pm}H_1)}. \quad (\text{B6})$$

[Equation \(B6\)](#) defines the two baroclinic deformation radii of the problem and  $h_i$  are the layer interfaces.

The equations are nondimensionalized by scaling distance on the first deformation radius ( $R_+$ ) and streamfunction by  $f_o R_+^2$ . The nondimensional normal equations are identical to [\(B5\)](#), where

$$\psi_b = \frac{H_1}{H_T} \psi_1 + \frac{H_2}{H_T} \psi_2 + \frac{H_3}{H_T} \psi_3$$

$$q_b = \frac{H_1}{H_T} q_1 + \frac{H_2}{H_T} q_2 + \frac{H_3}{H_T} q_3$$

$$h_{\pm} = h_1 + \gamma_{\pm} h_2$$

$$q_{\pm} = q_1 - q_2 + \gamma_{\pm} (q_2 - q_3)$$

$$(q_b^*, q_{\pm}^*) = f_o (q_b, q_{\pm})$$

$$(R_+^{-2}, R_-^{-2}) = \left( 1, \frac{R_+^{2*}}{R_-^{2*}} \right), \quad (\text{B7})$$

all unstarred variables are nondimensional and starred variables are dimensional. Each of [\(B5\)](#) has an associated Green's equation,

$$\nabla^2 G_b = \delta(\mathbf{x} - \mathbf{x}_o)$$

$$\nabla^2 G_{\pm} - R_{\pm}^{-2} G_{\pm} = \delta(\mathbf{x} - \mathbf{x}_o); \quad (\text{B8})$$

constrained by the same boundary conditions. Solutions of [\(B5\)](#) may then be written

$$z(\mathbf{x}_o) = \iint G^z(\mathbf{x}_o; \mathbf{x})q^z(\mathbf{x}) dA, \quad (\text{B9})$$

where  $z = \{\psi_b, \psi_\pm\}$ ,  $G^z = \{G_b, G_\pm\}$ , and  $q^z = \{q_b, q_\pm\}$ .

The meddy is modeled using point vortices. The  $q$  anomaly strength of each point vortex is taken from (B9); that is, the integral there is approximated by

$$\iint G(\mathbf{x}_o; \mathbf{x})q(\mathbf{x}) dA \approx \sum_{p=1}^{NV} G_p(\mathbf{x}_o; \mathbf{x}_p)q(\mathbf{x}_p)\delta A_p, \quad (\text{B10})$$

where the Green's function  $G_p$  is that forced by a Dirac delta function at location  $\mathbf{x}_p$ . The ‘‘strength’’ of the point vortex is given by  $q(\mathbf{x}_p)\delta A_p$ , where  $\delta A_p$  is the area of the original vortex now assigned to the point vortex  $p$ . The computational challenge of this problem is to obtain the Green's function solutions to (B5).

#### a. The barotropic solution

The barotropic solution is written as the sum of the barotropic flow at large  $\mathbf{r}$ , a singular part and a homogenous part

$$G_b = -U_oHy + \psi_s + \psi_h, \quad (\text{B11})$$

where the amplitude of the mean flow is  $U_o$ . The no-net-circulation constraint is satisfied trivially by the barotropic mode. The general homogenous solution is

$$\begin{aligned} \psi_h = & \sum_{m=-\infty}^{\infty} a_m r^{-|m|} e^{-im\theta} \\ & + \sum_{m=-\infty}^{\infty} g_m r^{|m|} e^{-im\theta} + d_o \log(r), \end{aligned} \quad (\text{B12})$$

where  $m$  is an integer and the coefficients  $a_m$  and  $g_m$  are complex. Note,  $g_m = d_o = a_o = 0$  by the boundary conditions. The quantity  $\psi_h$  is real, so  $a_m^* = a_{-m}$  and thus

$$\psi_h = 2 \sum_{m=1}^{\infty} r^{-m} [a_m^r \cos(m\theta) + a_m^i \sin(m\theta)], \quad (\text{B13})$$

where  $a_m^r, a_m^i$  denote the real and imaginary parts of  $a_m$ . This can be generalized by writing

$$\psi_h = \sum_{k=1}^{\text{NC}} \left\{ 2 \sum_{m=1}^{\infty} R_k^{-m} [a_{k,m}^r \cos(m\theta_k) + a_{k,m}^i \sin(m\theta_k)] \right\}, \quad (\text{B14})$$

where the subscript  $k$  denotes the  $k$ th cylinder,  $R_k$  the radial coordinate relative to the  $k$ th cylinder center ( $R_k = |\mathbf{r} - \mathbf{r}_k|$ ), and  $\theta_k$  the angular coordinate relative to the  $k$ th cylinder center.

Neglecting  $\psi_s$ , the NC boundary equations reduce to

$$c_{k_o} = 2 \sum_{k=1}^{\text{NC}} \left\{ \sum_{m=1}^{\infty} (|\mathbf{r}_{\delta k_o} - \mathbf{r}_k|)^{-m} [a_{k,m}^r \cos(m\theta_{\delta k_o,k}) + a_{k,m}^i \sin(m\theta_{\delta k_o,k})] \right\} - U_o H(y_{k_o} + a_{k_o} \sin\theta_{k_o}) \quad (\text{B15})$$

(Click the equation graphic to enlarge/reduce size)

for  $k_o = \{1, \text{NC}\}$ . In (B15),  $\mathbf{r}_k = (x_k, y_k)$  denotes the center of cylinder  $k$  and  $\mathbf{r}_{\delta k_o}$  a point on the boundary of the  $k_o$ th cylinder. The quantity  $\theta_{\delta k_o,k}$  is the angle of a point on the  $k_o$ th cylinder relative to the center of cylinder  $k$ .

If there is only one cylinder (NC = 1), the solution to (B15) can be obtained by a Fourier transform in  $\theta$ . The result is

$$c_1 = -U_o H y_1, \quad a_{1,1}^i = \frac{U_o H a_1^2}{2} \quad (\text{B16})$$

and all other coefficients vanish. The need for an iterative solution arises when there are several cylinders. Each cylinder cancels their barotropic pressure distribution using (B16), but those homogenous contributions “broadcast” their own pressure distributions across neighboring cylinders. These must be cancelled by other contributions to the coefficients.

Given a guess for the amplitudes, here called  $a_{k,m}^n$ , the pressure on the  $k_o$ th boundary left by these amplitudes is

$$\begin{aligned} c_{k_o} + U_o H (y_{k_o} + a_{k_o} \sin \theta_{k_o}) + 2 \sum_{k=1}^{\text{NC}} \sum_{m=1}^P \{ |\mathbf{r}_{\delta k_o} - \mathbf{r}_k|^{-m} [a_{m,k}^{r,n} \cos(m\theta_{\delta k_o,k}) + a_{m,k}^{i,n} \sin(m\theta_{\delta k_o,k})] \} \\ = \delta G_b [x_{k_o} + a_{k_o} \cos(\theta_{\delta k_o}), y_{k_o} + a_{k_o} \sin(\theta_{\delta k_o})], \end{aligned} \quad (\text{B17})$$

*(Click the equation graphic to enlarge/reduce size)*

where  $P$  is the number of retained azimuthal modes. The “correct” amplitudes  $a_{k,m}$  yield  $\delta G_b = 0$ , although in general the guess  $a_{k,m}^n$  will not satisfy this constraint. Therefore, a correction to the coefficients,  $\delta a_{k,m}^{[r,i]n+1}$ , is computed from the residual in (B17):

$$\begin{aligned} \delta G_{b,k_o} = 2 \sum_{k=1}^{\text{NC}} \sum_{m=1}^P \{ |\mathbf{r}_{\delta k_o} - \mathbf{r}_k|^{-m} [ \delta a_{m,k}^{r,n+1} \cos(m\theta_{\delta k_o,k}) \\ + \delta a_{m,k}^{i,n+1} \sin(m\theta_{\delta k_o,k}) ] \}. \end{aligned} \quad (\text{B18})$$

The right-hand side of (B17) is approximated by using the contribution from cylinder  $k_o$  only:

$$\begin{aligned} \delta G_{b,k_o} \approx 2 \sum_{m=1}^P \{ |\mathbf{r}_{\delta k_o} - \mathbf{r}_{k_o}|^{-m} [ \delta a_{m,k_o}^{r,n+1} \cos(m\theta_{\delta k_o,k_o}) \\ + \delta a_{m,k_o}^{i,n+1} \sin(m\theta_{\delta k_o,k_o}) ] \}. \end{aligned} \quad (\text{B19})$$

A Fourier transform in  $\theta$  of (B19) gives the corrections to the coefficients. The  $(n+1)$ th estimate of the total coefficient is  $a_{k_o,m}^{[r,i]n+1} = a_{k_o,m}^{[r,i]n} + \delta a_{k_o,m}^{[r,i]n+1}$ . The truncation of the exact equation in (B18) to its “preconditioned” form in (B19) implies the coefficients  $a_{k_o,m}^{[r,i]n+1}$  will not exactly cancel the pressure structure on the cylinder boundary; therefore, the procedure is repeated until the corrections exceed a stopping criterion like

$$\sum_{k=1}^{\text{NC}} \sum_{m=1}^{P/2} \left( \frac{|\delta a_{k,m}^{r,n+1}|}{|a_{k,m}^r|} + \frac{|\delta a_{k,m}^{i,n+1}|}{|a_{k,m}^i|} \right) < \epsilon. \quad (\text{B20})$$

Vanishing amplitudes are used at the beginning of the integration. After that, the iterations are started using the amplitudes from the previous time step. Rather stringent stopping criteria, like  $\epsilon = O(10^{-11})$ , are achieved in six to eight iterations.

Including singular solutions is straightforward. Given  $\text{NV}(i)$  vortices in layer  $i$ , each at known locations  $\mathbf{x}_j$ , these project onto  $\sum_{i=1}^3 \text{NV}(i)$  delta function contributions to each equation. Considering the collection of point vortices,

$$\psi_s = \sum_{i=1}^3 \sum_{j=1}^{\text{NV}(i)} \frac{\alpha_{i,j}}{2\pi} \ln(|\mathbf{x} - \mathbf{x}_{i,j}|), \quad (\text{B21})$$

where the  $\alpha_{i,j}$  are associated with the “strength” of the vortices. Each of these singular vortices broadcasts a pressure distribution across the cylinders and the above iterative technique is used to cancel them.

### *b. Baroclinic solutions*

The procedure here is similar to the above; that is, the baroclinic mode is written

$$G = h_s + h_h, \quad (\text{B22})$$

where  $G$  denotes ( $G_{\pm}$ ),  $h_s$  the singular contributions from the vortices and  $h_h$  the homogenous solutions of (B5). The singular solutions are written as

$$h_s = - \sum_{l=1}^3 \sum_{p=1}^{NV(l)} \frac{s_{l,p}}{2\pi} K_0 \left( \frac{|\mathbf{r} - \mathbf{r}_{l,p}|}{R} \right), \quad (\text{B23})$$

where  $R$  is the appropriate nondimensional deformation radius and  $K_0$  is the zeroth modified Bessel function of the first kind. The quantity  $s_{l,p}$  is the vortex strength of the  $\psi$ th vortex in layer  $l$ , as it appears to the baroclinic mode. The homogenous solution to (B5) is

$$h_h = \sum_{k=1}^{\text{NC}} \left\{ b_{k,o}^r K_0 \left( \frac{|\mathbf{r} - \mathbf{r}_k|}{R} \right) + \sum_{m=1}^{\infty} K_m \left( \frac{|\mathbf{r} - \mathbf{r}_k|}{R} \right) \times [b_{k,m}^r \cos(m\theta_k) + b_{k,m}^i \sin(m\theta_k)] \right\}, \quad (\text{B24})$$

where  $K_m$  is the  $m$ th modified Bessel function of the first kind.

The major difference here is that the singular and homogenous baroclinic solutions can “broadcast” circulation as well as pressure. This must be cancelled on a cylinder by the  $K_0$  contribution to the homogenous solutions.

Given a guess for the  $b_{k,m}$  coefficients, the azimuthal velocity on the cylinder boundaries is computed and summed to yield an estimate of the residual circulations,  $S_k^n$ . Additional corrections to the  $K_0$ th coefficients are then computed according to

$$\frac{-2\pi\delta b_{k,o}^{n+1}}{R} K_1 \left( \frac{a_k}{R} \right) = S_k^n; \quad (\text{B25})$$

$$b_{k,m}^{n+1} = b_{k,m}^n + \delta b_{k,m}^{n+1} \quad (\text{B26})$$

is then enforced, and the iteration continued until a stopping criterion, like (B20), is met.

### c. Special issues

Two cases requiring special attention are for vortices very close to one another in the horizontal and vortices very near the cylinder boundaries. In the former, if the separations were less than a preset value (typically  $0.01R_+$ ), analytically generated small argument expansions were used in place of the Bessel functions. The latter case could result in the spurious penetration of vortices through the cylinder boundaries. Vortex location relative to cylinder boundaries was monitored and, if penetration was noted, the offending vortex was “pushed” radially outward to the vortex boundary. The number of occurrences of this behavior was a function of the time step, and could be controlled by reducing it.

---

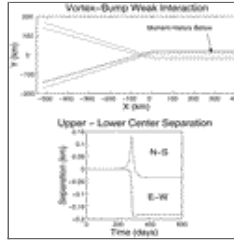
## Figures





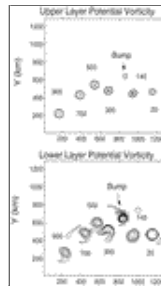
[Click on thumbnail for full-sized image.](#)

FIG. 1. Meddy–topography interaction. This is a westward-looking view of the Great Meteor Seamount Chain as seen by meddies. Several seamounts appear and the oval indicates the average depth and size of a typical meddy



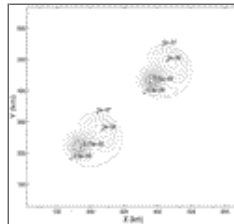
[Click on thumbnail for full-sized image.](#)

FIG. 2. Point vortex interaction with a bottom bump. (upper panel) Upper-layer point vortex trajectories and (lower panel) the zonal and meridional separation between the upper- and lower-layer point vortices from the experiment indicated by the upper panel arrow. No dipole moment exists prior to the interaction; postinteraction, the dipole moment is finite and fixed in time



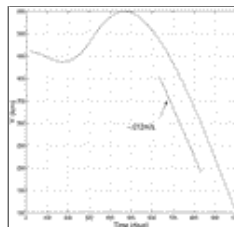
[Click on thumbnail for full-sized image.](#)

FIG. 3. Vortex–topography weak interaction from a finite-difference model: upper-layer  $q$  (upper panel) and lower-layer  $q$  (lower panel). This is a composite of six different plots. The dates of the plots in days appear by each vortex snapshot. The location of the bottom topography appears in both panels. The topography includes a bound anticyclonic vortex that is largely steady for the duration of the experiment and thus not labeled with a date



[Click on thumbnail for full-sized image.](#)

FIG. 4. Composite of upper and lower  $q$  fields from a scattered vortex. Results from days 700 and 900 are shown, indicating the stability of the structure and the induced propagation speed. Further the structure is hetonlike. The approximate southward translation speed is  $0.01 \text{ m s}^{-1}$



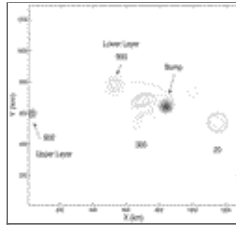
[Click on thumbnail for full-sized image.](#)

FIG. 5. Upper meridional  $q$  centroid trajectory as a function of time. The slope of the included line is  $0.012 \text{ m s}^{-1}$ , which roughly parallels the track



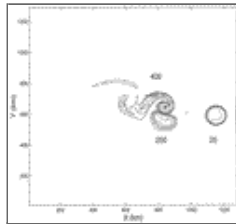
[Click on thumbnail for full-sized image.](#)

FIG. 6. Upper zonal  $q$  centroid trajectory. The slope of the included line is  $-0.013 \text{ m s}^{-1}$ , indicating a considerable impedance of vortex propagation by self-interaction mechanisms



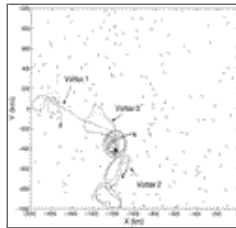
[Click on thumbnail for full-sized image.](#)

FIG. 7. A strong vortex–topography interaction. Composite of three separate lower-layer  $q$  plots is shown; the times of the plots in days appears next to the vortices. A plot of the upper  $q$  anomaly for the later date appears as well and shows the disassociation between the upper and lower vortex expressions. This interaction leaves the lower anomaly intact, if distinct from the upper anomaly



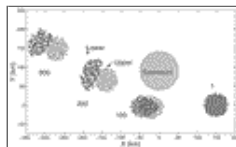
[Click on thumbnail for full-sized image.](#)

FIG. 8. A very strong vortex–topography interaction. Three plots of the lower  $q$  anomaly are shown, and the associated dates in days are indicated. The latter date shows the destruction of the lower-layer vortex, which has been sheared out into a zonal tendril. The upper-layer vortex at this time (not shown) is no longer associated with the lower center, and subsequently propagates zonally



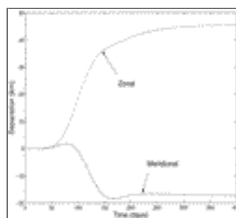
[Click on thumbnail for full-sized image.](#)

FIG. 9. A weak interaction between a vortex and a seamount. The locations of the point vortices are shown from four different dates (the time in days of the snapshots appears next to the vortices), and the seamount location is indicated. The vortex centers separate because of the interaction and the long-term evolution is nearly steady



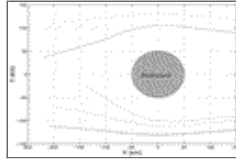
[Click on thumbnail for full-sized image.](#)

FIG. 10. Vortex trajectories in the vicinity of distributed topography. The locations of the bumps are indicated by the asterisks. Their amplitude is random, but centered on a height of 100 m. Three trajectory sets are shown; both upper and lower point vortex paths appear. Their initial locations are close and all indicated by the mark at  $(-1000 \text{ km}, -250 \text{ km})$ . Their subsequent trajectories are characterized by rapid separation in space, and their final locations are also indicated by a cross. Note the twists and kinks in the computed trajectories



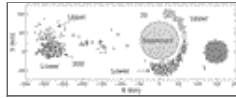
[Click on thumbnail for full-sized image.](#)

FIG. 11. Centroid separation time history. Both zonal and meridional components appear, with the former dominating in size. Positive values denote the upper layer leading the lower layer



[Click on thumbnail for full-sized image.](#)

FIG. 12. Centroid trajectories from several vortex-seamount interactions from weak interactions. The seamount location is indicated and results from 200 days of integration are shown



[Click on thumbnail for full-sized image.](#)

FIG. 13. A strong interaction between a vortex and a seamount. Three different plots are shown; the dates of the plots are shown. Note the disruption of the vortex by the interaction, but its remarkable capacity for reorganizing into a heton configuration

*Corresponding author address:* William K. Dewar, Department of Oceanography, The Florida State University, Tallahassee, FL 32306. E-mail: [dewar@ocean.fsu.edu](mailto:dewar@ocean.fsu.edu)

<sup>1</sup> Note that dipole moments are usually associated with barotropic vortices in the literature. Here we are discussing baroclinic settings in which the baroclinic structure is integrally involved in the moment generation.

<sup>2</sup> M. Stern (2000, personal communication) has shown that (10) is comparable to, but not exactly equal to, the eddy propagation speed. The actual propagation speed requires computing the motion of the vortex boundary, rather than the center of mass.

<sup>3</sup> The term “weak” is used in the informal sense of [Stern \(1999\)](#) and denotes a vortex–topography interaction characterized by the pair remaining locked together. Conversely, a “strong” interaction is one in which the upper and lower point vortices are stripped apart. An analogous, informal definition will also apply when continuously distributed vortices are considered later.

[top](#) ▲



© 2008 American Meteorological Society [Privacy Policy and Disclaimer](#)  
Headquarters: 45 Beacon Street Boston, MA 02108-3693  
DC Office: 1120 G Street, NW, Suite 800 Washington DC, 20005-3826  
[amsinfo@ametsoc.org](mailto:amsinfo@ametsoc.org) Phone: 617-227-2425 Fax: 617-742-8718  
[Allen Press, Inc.](#) assists in the online publication of AMS journals.